10

FRACTURE MECHANICS AND COMPRESSIVE FAILURE

10.1 EXPERIMENTAL OBSERVATIONS OF CRACK PROPAGATION AND DAMAGE

Concrete has much higher strength in compression than in tension. As discussed in Chapter 4, many initial flaws exist in a cementitious matrix as well as at the interface between coarse aggregate and the matrix due to segregation during casting and shrinkage and thermal cracking. Propagation of these cracks is responsible for the so-called compressive failure of concrete.

Many studies have been previously conducted to observe propagation of cracks for concrete under compression. Hsu et al.[1] and Shah and Chandra[2] have observed internal cracks of compressive specimens with a microscope and x-ray photographs. Shah and Sankar[3] tested a series of concrete cylinders of 75 mm (3 in.) diameter and 150 mm (6 in.) height under uniaxial compression using a closed-loop testing machine. Axial displacement and diametric deformations at different levels of specimen height (locations A, B, and C in Fig. 10-1) were measured during testing. A typical compressive stress–axial displacement relationship obtained is shown in Fig. 10-1a, and corresponding diametric deformations at various loading levels along the specimen height are indicated in Fig. 10-1b. It is seen that the lateral displacement is basically uniform along the specimen height up to about 80% of the peak load (point 2). After point 2, the lateral deformation at location B increases much faster than those at locations A and C. This indicates that to some extent strain localization appears in the vicinity of location B. Shah and Sankar[3] also monitored crack patterns in both transverse and longitudinal directions using petrography techniques. Specimens loaded to each deformation level were sectioned, one transversely and one longitudinally. Slices $1\frac{1}{2}$ in. (12 mm) thick

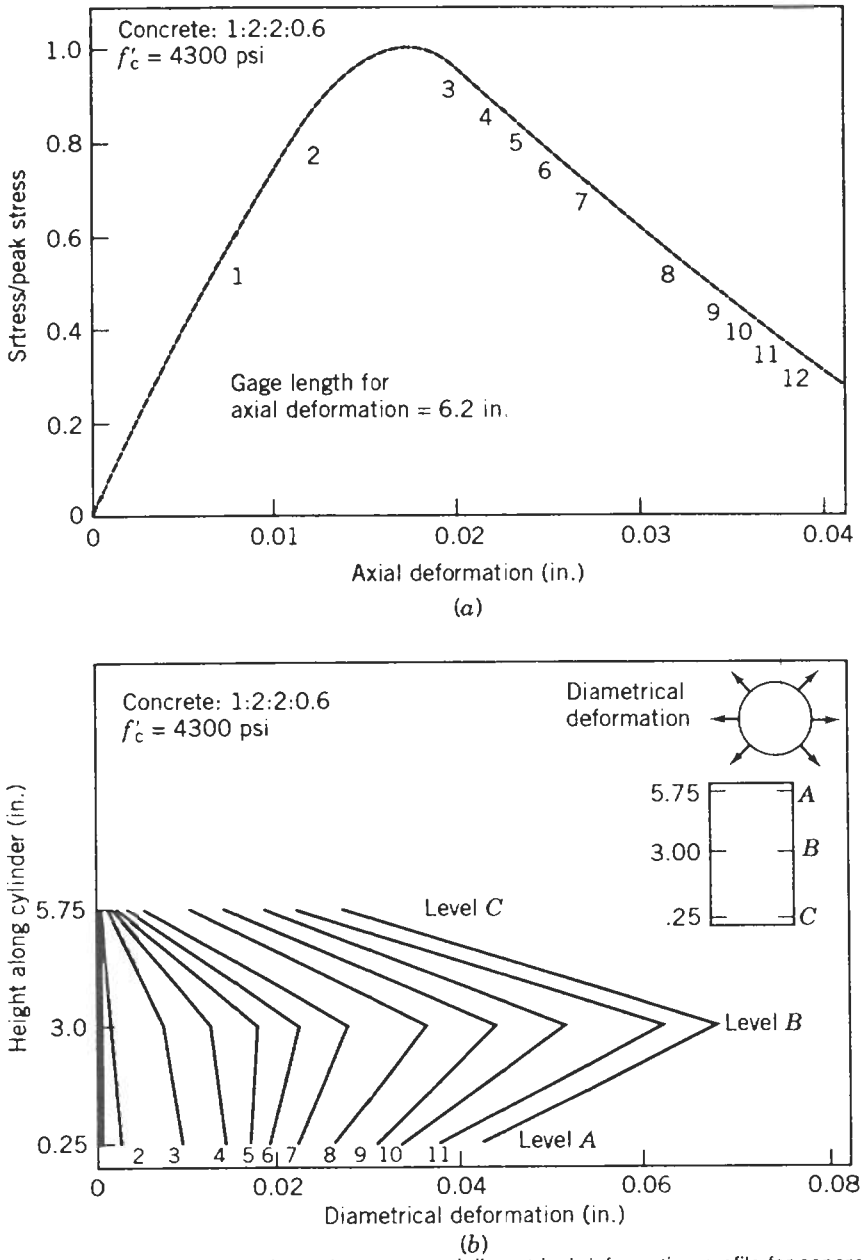

Figure 10-1 Load–axial deformation curve and diametrical deformation profile for concrete cylinder under uniaxial compression.[3]

were cut from the center of the specimen using a diamond saw. The obtained crack patterns for different loading stages are shown in Fig. 10-2. It was reported based on these observations that the extent of cracking up to about 83% of peak load is primarily limited to bond cracking between coarse aggregates and mortar matrix (Fig. 10-2*a*). These bond cracks are uniformly distributed in both transverse and longitudinal directions. When the applied stress continuously increases, these bond cracks start to coalesce into continuous cracks that can be seen at the two edges of the longitudinal section, as indicated in Figs. 10-2*b*, *c*. Cracking is uniform and extensive in both longitudinal and transverse sections further into the postpeak region (Fig. 10-2*d*). Shah and Chandra[2] observed a significant increase of specimen volume after about 80% of the peak load. A similar strain localization was also observed by Torrenti et al.[4,5] using stereophotogrammetry and speckle laser.

Maji and Shah[6] used laser holography to observe initiation and propagation of cracks in model concrete specimens. Results obtained are illustrated in Fig. 10-3. Cracks initiate at the interface between aggregates and cementitious matrix and then propagate into the matrix as applied load increases. Crack paths near the peak stress are basically in the same direction as the applied load.

Based on these experimental observations, the failure process of a uniaxial compressive concrete specimen may be summarized as in Fig. 10-4. The compressive stress–strain relationship may be divided into several stages. Stress initially linearly increases with strain. The microflaws start to open at point *A*, which is approximately 30% of peak stress. The interfacial flaws propagate at point *B* (about 50% of the peak stress). These bond cracks, which are isolated and uniformly distributed over the whole specimen, propagate in different directions based on the shapes of the aggregates. These bond cracks propagate into the mortar matrix and coalesce as a single crack or several major cracks that are in the direction of the applied compressive load at about 80% of the peak stress (point *C*). This is strain localization in compression. The beginning of the strain localization accelerates failure of the specimen. These major cracks stably propagate, and one of them reaches its critical length at point *D*. As a result, the specimen exhibits its peak compressive stress. After the peak stress, the major cracks automatically propagate even though the applied load decreases. A softening type of stress–strain curve is usually observed for the compressive failure of concrete. Approximately, the specimen continuously contracts up to point *C*. However, the volume of the compressed concrete starts to increase rather than contract after pont *C*.[2,7] Although Poisson's ratio slightly increases as the load is applied, its value suddenly greatly increases approximately after point *C*. It is noted that for high-strength concrete, since the interfacial bond is improved by the use of cementitious materials such as silica fume, cracks may not initiate from the interfacial bond and some cracks may penetrate through aggregates.

When a uniaxial compressive specimen is tested, some lateral restraint stress may develop at the machine–specimen boundary due to different deformations between the steel loading platen and concrete.[8] The crack pattern (failure mode)

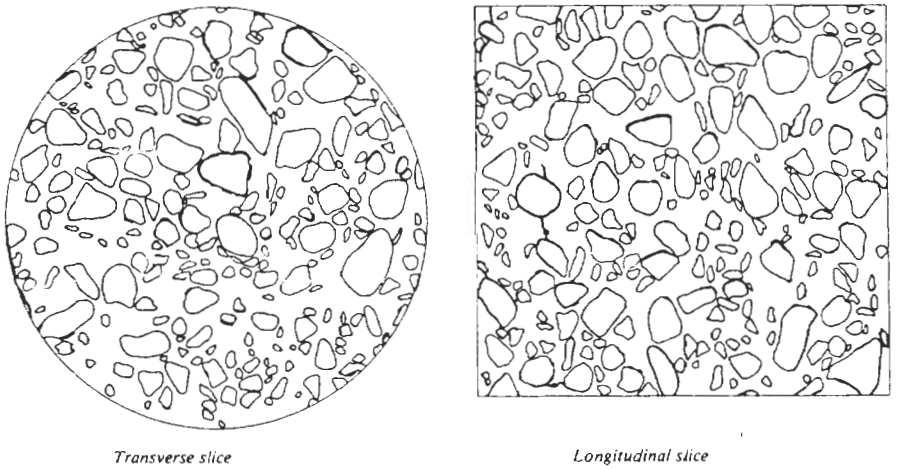

(*a*)

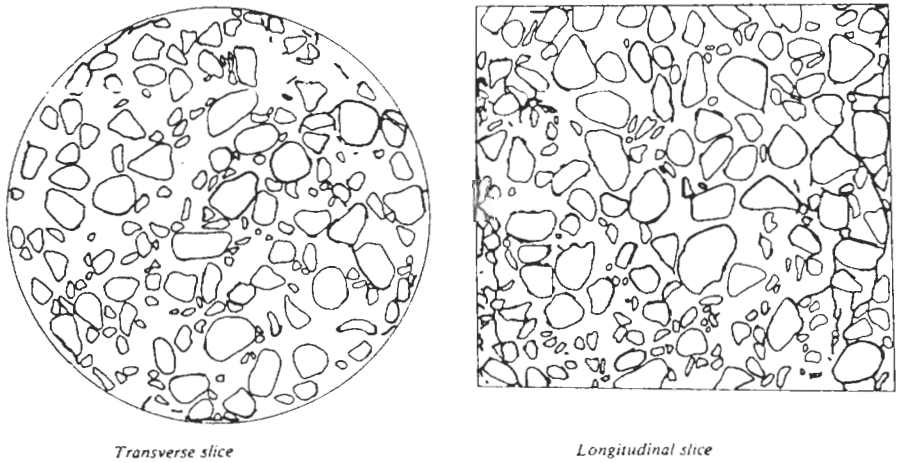

(*b*)

Figure 10-2 Transverse and longitudinal crack patterns at different loading stages: (*a*) up to 83% of the peak load, (*b*) up to the peak load, (*c*) up to 93% of the peak stress in the post-peak region, and (*d*) up to 81% of the peak stress in the post-peak region.[3]

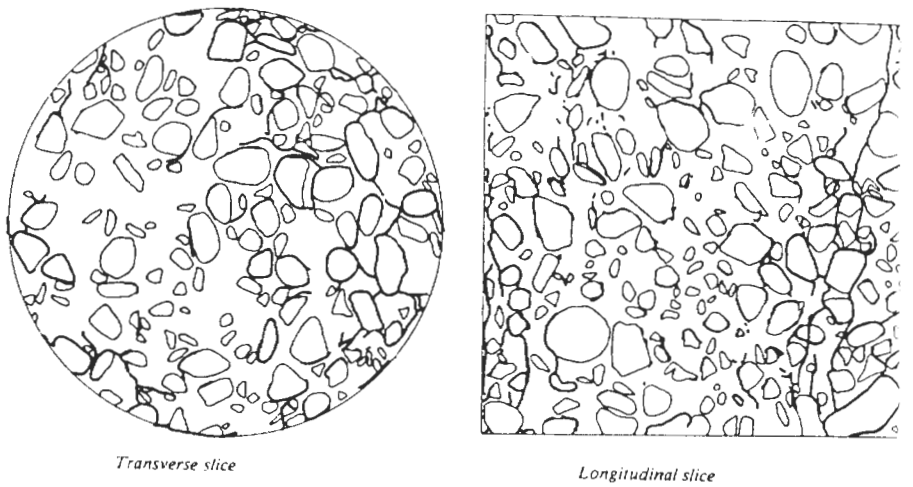

(*c*)

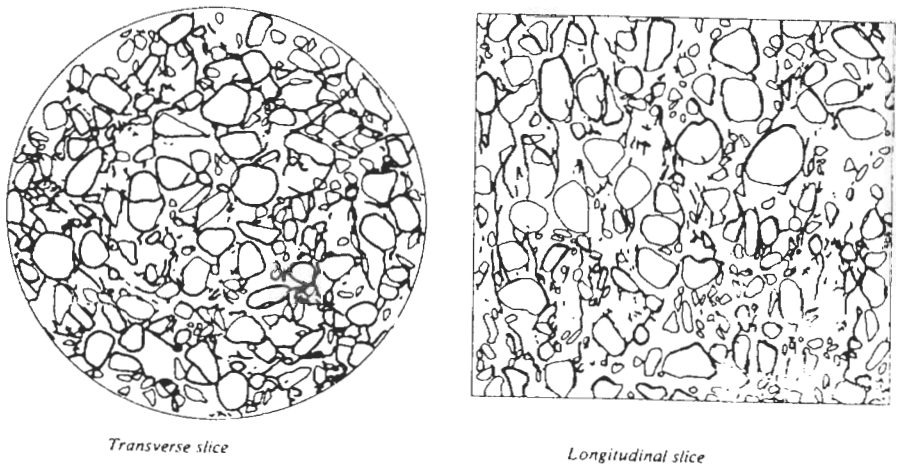

(*d*)

Figure 10-2 (*Continued*)

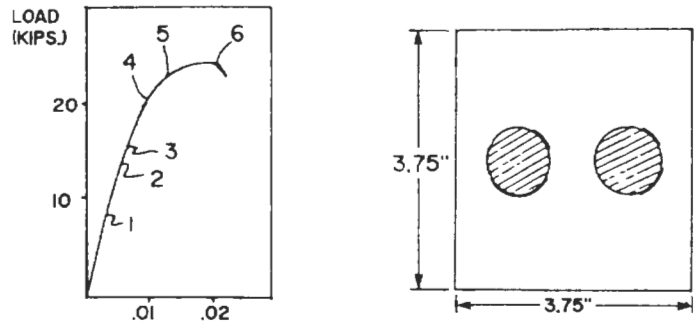

(a) (b)

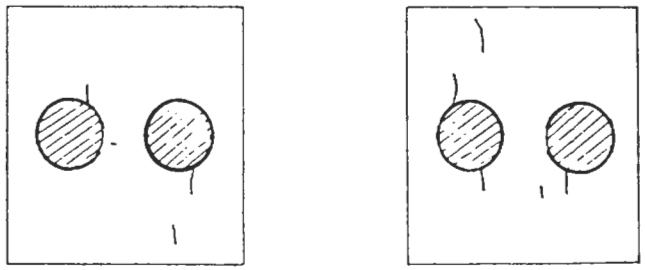

(c) (d)

Figure 10-3 Propagation of cracks in model concrete plate under uniaxial compression observed by laser holographic interferometry: (*a*) load displacement curve, (*b*) crack pattern at point 1, (*c*) crack pattern at point 2, (*d*) crack pattern at point 3, (e) crack pattern at point 4, (*f*) crack pattern at point 5 and (*g*) crack pattern at point 6.[5]

of a compressive specimen is influenced by this lateral restraint stress because it results in triaxial compressive stress states at the end regions of the specimen. These triaxial stress states arrest cracking in the end regions, which may delay or prevent strain localization and formation of macrocracks. Therefore, when plain steel loading platens are used for testing of a short specimen, a hourglass-type failure mode as shown in Fig. 10-5*a* is usually obtained. This type of failure mode cannot be used to characterize compressive failure of concrete. The influence of the lateral restraint stress can be minimized by using various mechanisms such as a brush-type loading device or lubricants. In this case, a significant amount of prominent vertical splitting cracks accompanied by some

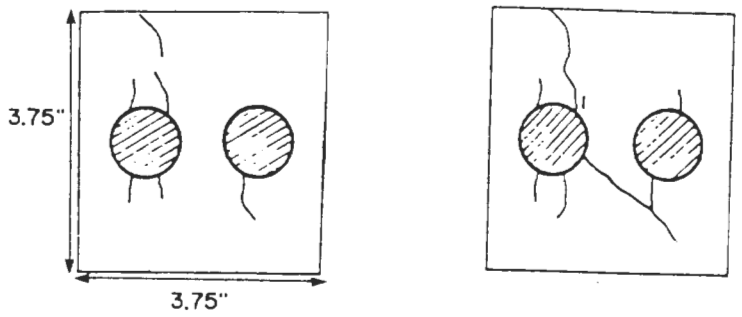

(e) (f)

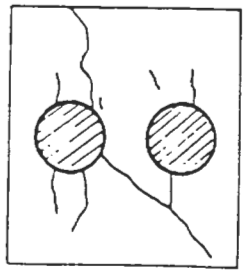

(g)

Figure 10-3 (*Continued*)

shear cracks are observed, as shown in Fig. 10-5*b*.[8,9] The effect of the lateral restraint stress can also decrease by increasing the slenderness of the tested specimen. Failure due to a single shear crack has been reported for slender specimens loaded using a hinged platen, as shown in Fig. 10-5*c*.[9]

Based on the above discussion, in a manner similar to tensile failure, the compressive failure of concrete is characterized by a strain localization evidenced by coalescence of one or several major cracks accompanied by sudden increase of Poisson's ratio. The major cracks formed after the strain localization are in directions of local maximum principal compressive stress, which globally coincide with the applied compressive load, rather than in a direction perpendicular to the applied force in tension. Since a crack results from tensile stresses developed primarily due to the effect of Poisson's ratio, several major cracks, instead of a single crack in the case of tension, are often observed after

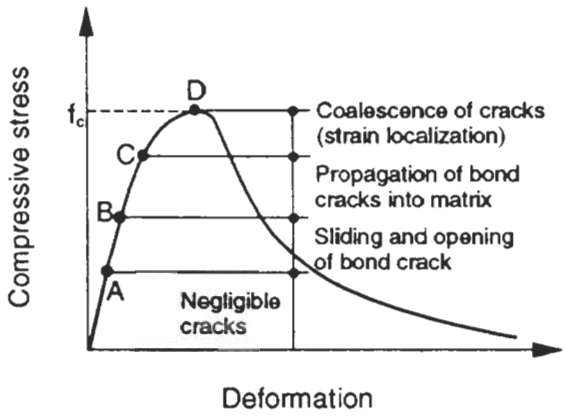

Figure 10-4 Stages of crack propagation in concrete under uniaxial compression.

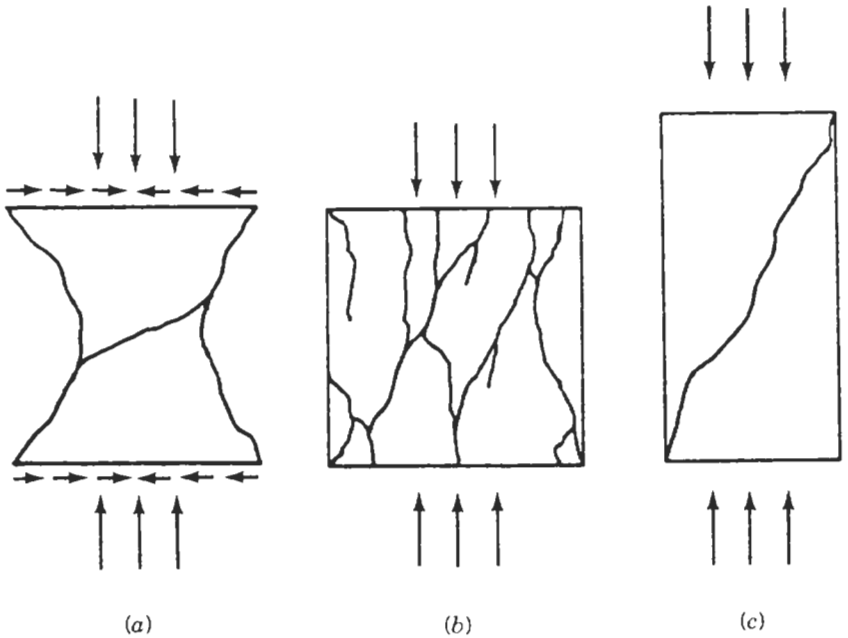

Figure 10-5 Failure modes of concrete specimens under uniaxial compression.[8,9]

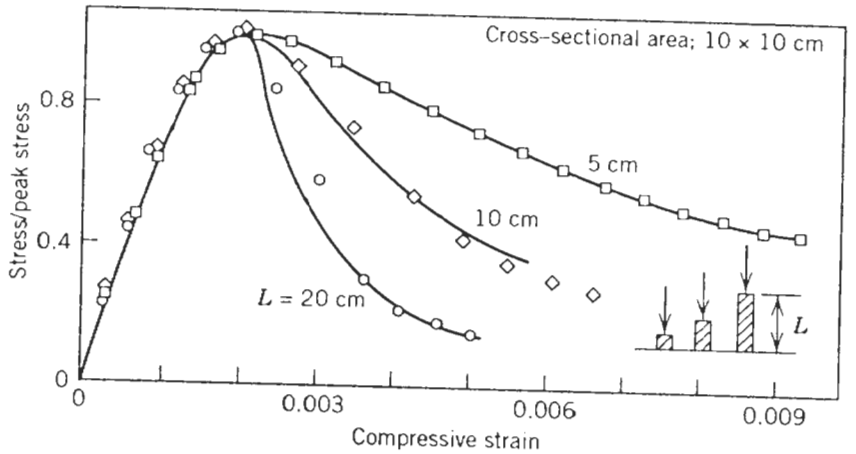

Figure 10-6 Influence of specimen height on uniaxial compressive stress–strain curves.[9]

the strain localization. The presence of strain localization allows one to use fracture mechanics to describe the failure behavior of concrete under compression.

The fact that fracture mechanics is a suitable approach to describe compressive failure of concrete is confirmed by experimental results reported by van Mier,[9] as shown in Fig. 10-6. His results indicate that postpeak compressive stress–strain curves depend on the height of prismatic specimens. Specimens with different heights have almost identical stress–strain behavior up to peak stress. However, longer specimens exhibit less strain after the peak stress compared to shorter specimens. This experimental observation indicates that many previous constitutive models[10,11] based on softening types of stress–strain relationships may not be appropriate for concrete. On the other hand, fracture mechanics can be used to reasonably describe the observed strain localization. An extensive review of experimental and theoretical studies on compressive failure of concrete has been given by Vonk.[12] Various approaches for compressive failure of concrete based on fracture mechanics will be discussed in this chapter.

10.2 FRACTURE MODELS FOR FAILURE RESULTING FROM INTERFACIAL BOND CRACKS

Both interfacial cracks and matrix voids exist in concrete before loading. A major crack usually initiates from an interfacial crack. This may be due to the facts that (i) the size of an interfacial crack is usually much larger than that of the matrix voids and (ii) the interfacial layer (transition zone) has a poor microstructure that results in a weaker fracture resistance.[13] The presence of the

interfacial transition zone greatly influences the fracture behavior of concrete. Concrete may be regarded as a three-phase material consisting of aggregate, cementitious matrix, and an interfacial transition zone.[14]

Since the weakest link in concrete is the interfacial bond layer, many investigations have been conducted to study the microstructure and mechanical properties of the interfacial transition zone. Hsu and Slate[15] studied the tensile bond strength between aggregate and paste or mortar. They reported that for different types of aggregates the tensile bond strength ranges approximately from 40 to 70% of that for the paste or mortar. Shah and Winter[16] used a unit consisting of a circular-cylindrical piece of aggregate, an interfacial thin layer, and a cementitious matrix, as shown in Fig. 10-7, to simulate structural behavior of concrete under uniaxial compression. In this figure the ratio of d_1/r_a depends primarily on the relative amounts of aggregate and mortar in a given mix, and its value ranges from 0.2 to 0.6 for conventional concrete.[17] A theoretical model to predict compressive stress–strain curves of concrete was derived based on such a unit. In Shah and Winter's model[16] both the aggregate and the matrix were assumed to be linear elastic materials, whereas the interfacial bond was assumed to follow an elastic-plastic stress–strain relationship. Initially, the interfacial bond between the aggregate and the matrix is intact,

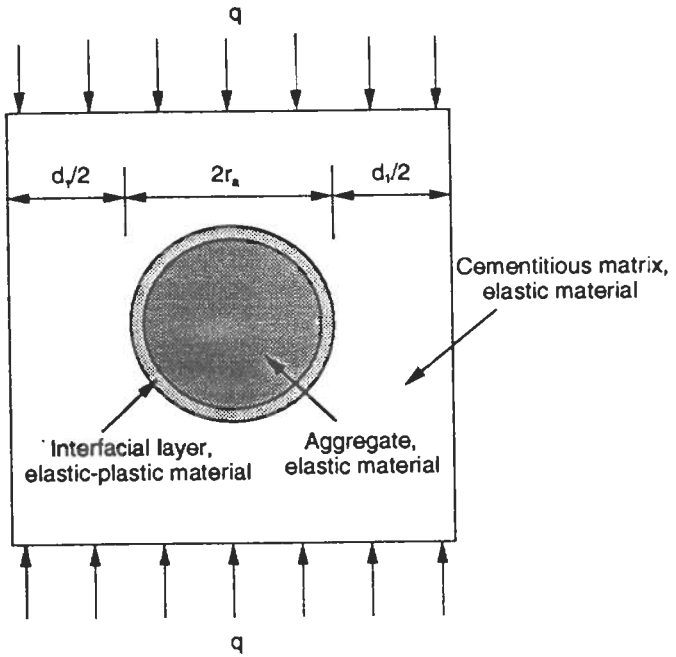

Figure 10-7 Structural unit to model compressive response of concrete proposed by Shah and Winter.[16]

and the unit behaves linearly elastically. Since the bond layer has a lower strength, some part of the bond layer reaches its yield stress at a certain load level. This yielded zone in the bond layer, which can be regarded as a bond crack, propagates with increasing load. Failure of the bond layer is described by Mohr's failure theory. After the bond layer starts to yield, the global relationship stress–strain becomes nonlinear. The above procedure was analytically implemented by Shah and Winter.[16] Their model is capable of predicting the stress at which the bond cracks initiate and the matrix cracking begins. Nonlinear stress–strain curves of concrete under uniaxial compression result from the progressive bond cracking. Note that in this model only the interfacial debonding was simulated, and the effect of matrix cracking on the stress–strain response was neglected. Some of the bond cracks propagate into the cementitious matrix when strain localization begins, and isolated bond cracks at interfaces of different aggregates coalesce into one or several major cracks. Since the matrix cracking has a significant effect on the stress–strain behavior after the strain localization, this model may only be valid up to the beginning of strain localization (at about 80% of the peak stress).

Shah and Winter's model was significantly improved by Buyukozturk et al.[18] They proposed a unit including nine cylindrical aggregate pieces placed in three symmetric rows about horizontal and vertical axes, as shown in Fig. 10-8. A plane-stress FE analysis was applied to the three different phases of the materials to obtain stress–strain curves of the unit. Since nine aggregate pieces were included, their model can be used to study the coalescence of isolated bond cracks at interfaces of different aggregates after strain localization. Results from the FE analysis indicated that cracks first initiate at weak bond layers surrounding different aggregates, and at about 70% of the peak load, these bond cracks start to propagate into the cementitious matrix. As the applied load further increases, several major cracks appear, and the unit fails at the peak stress. They reported that predicted crack patterns coincided with experimental observations and that the predicted and observed axial stress–strain curves up to the peak stress were in good correlation. Palaniswamy and Shah[19] further applied this nine-aggregate-piece model to concrete under cylindrical triaxial stresses. It is noted that the interfacial layer may not be weak for high-strength concrete due to the use of silica fume. Therefore, this approach may not be applied effectively to high-strength concrete.

Vonk[12] has used a more complicated FE model to study failure of compressive specimens due to interfacial cracks.

10.3 MULTILEVEL FRACTURE MODEL OF ZAITSEV AND WITTMANN

10.3.1 Concrete as Multilevel Hierarchy System

Zaitsev and Wittmann[20] and Zaitsev[21] proposed a multilevel fracture model to describe compressive failure of concrete. Based on its microstructure, a ce-

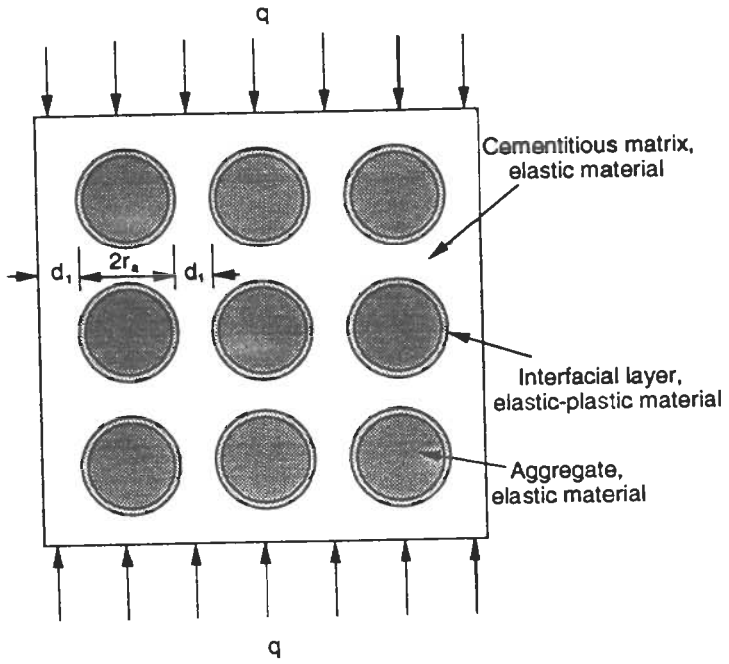

Figure 10-8 Structural unit to model compressive response of concrete proposed by Buyukozturk et al.[18]

mentitious material may be divided into macrolevel, mesolevel, and microlevel for predicting its fracture behavior. Inhomogeneity on each level was represented by a type of inclusion. Linear elastic fracture mechanics was used to describe fracture at these different material levels. To assure validity of LEFM, the minimum dimension of the representative volume element (RVE) was required to be at least four times the maximum grain size. The inhomogeneity on the macrolevel was given by "big" inclusions such as coarse aggregates. The typical linear dimension of the RVE for this level was assumed to be on the order of magnitude of 100 mm. On the mesolevel, the mortar volume between aggregates was considered. Inclusions on this level were average grains of fine aggregates. The typical linear dimension of the RVE for the mesolevel was an order of magnitude of 10 mm. On the microlevel, hardened cement paste volumes between fine aggregates were considered. A main inhomogeneity was represented by big capillary pores. The maximum size of these pores may have an order of magnitude of 0.01 mm, and the typical linear dimension of the RVE for the microlevel may be approximately 0.5 mm.

10.3.2 Crack Propagation in Hardened Cement Paste

Crack propagation in a hardened cement paste is based on the microlevel consideration and may be described by the simplified model shown in Fig. 10-9*a*. The big pores on the microlevel were modeled by a set of circular holes with a radius of r_h, and two line cracks were assumed to associate with each hole. It was simply assumed that all the cracks are coplanar and are in the most dangerous orientation (the direction of applied compressive load). When the load increases, cracks start to propagate in a stable way that required $K_I = K_{Ic}$, where K_I is the stress intensity factor and K_{Ic} is the critical stress intensity factor. This condition can be described by the expression

$$q = -K_{Ic}\sqrt{\frac{\pi}{4r_h}\frac{(1+\lambda_h)^7}{(1+\lambda_h)^2-1}} \tag{10.1}$$

where $\lambda_h = l_h r_h$ is the relative crack length and q is the applied compressive load, which is negative for compression. The detailed derivation of Eq. (10.1) and a more general condition with different crack lengths at both sides of a

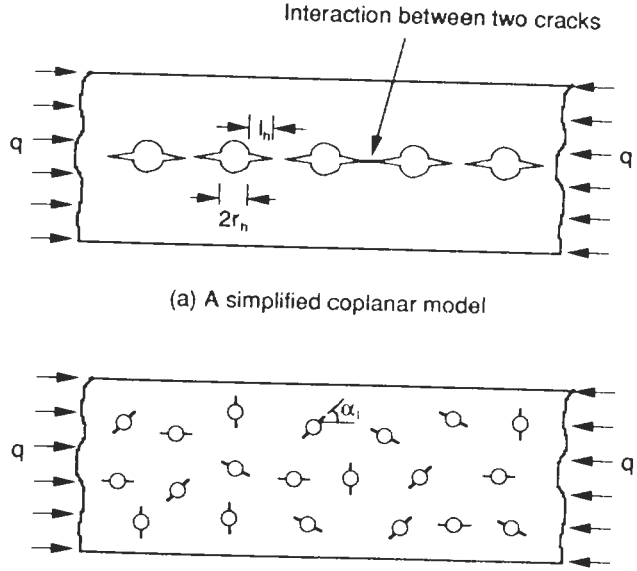

Figure 10-9 Models for structure of hardened cement paste.[20]

hole are also given by Zaitsev.[21] When the load further increases, cracks begin to interact. Beyond a certain load the crack propagation becomes unstable and the specimen fails.

In the above simplified analysis, a series of coplanar cracks is assumed. However, in a real hardened cement paste, cracks are oriented at random. It may be assumed that all pores are statistically uniformly distributed, as shown in Fig. 10-9*b*. Each pore may be assumed to have two preexisting cracks, and the length of the cracks is uniformly distributed within the range of $0 < l_h < 2r_h$. The angle of crack orientation with respect to the applied load, α_i, is also uniformly distributed within the limits between 0 and 2π. The interaction of cracks was taken into account by assuming that two cracks will interact and coalesce if α_1 and α_2 are both below $\pi/6$ or α_1 is below $\pi/6$ while α_2 is above $5\pi/6$. The random structure was created by a computer program. If crack propagation is studied by the Monte Carlo method, the results are similar to those obtained by using the one-dimensional model shown in Fig. 10-9*a*.

For both model structures (the coplanar cracks and the two-dimensional crack arrangement shown in Fig. 10-9), the equations describing crack propagation for stable crack propagation can be written in a general form as

$$q = -\frac{K_{1c}}{\sqrt{2r_h}} g(\lambda_h) \tag{10.2}$$

where $g(\lambda_h)$ is a function of the related crack length λ_h.

Simulation of crack propagation as described above makes it possible to estimate the effect of pore size distribution on the fracture mechanism, mechanical strength, and strain behavior of hardened cement paste. It has been found that by increasing the mean size of pores while keeping the quantity constant, the ultimate load will decrease.[20] It is noted that a Griffith-type fracture criterion was used for both Eqs. (10.1) and (10.2) because only the critical stress intensity factor K_{1c} was involved.

10.3.3 Crack Propagation in Concrete

Fracture of concrete may be treated on the mesolevel of the hierarchical system of the structure of materials. The main defects in concrete result from bleeding, shrinkage, and other processes in fresh and hardening concrete. Most of these cracks are interfacial bond cracks between hardened cement paste and coarse aggregates. The actual structure of concrete may be modeled by a unit thickness elastic plate containing inclusions (coarse aggregate particles). Aggregates with random polygonal shape are randomly distributed in a homogeneous matrix.

First consider a randomly inclined crack in a homogeneous plate loaded at infinity, as shown in Fig. 10-10. It can be shown that as the compressive load increases, two branching cracks of mode I may be created at the ends of the

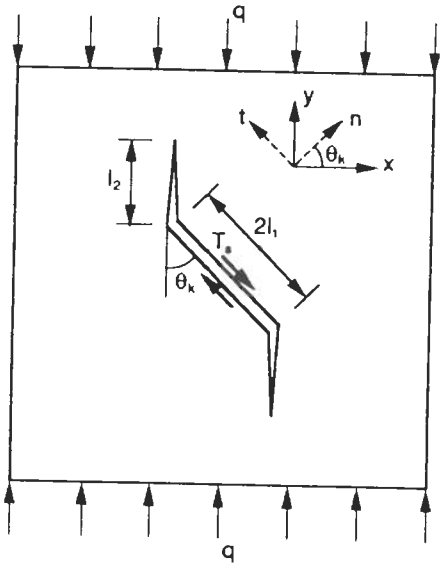

Figure 10-10 Development of branching cracks from inclined crack.[20]

initial inclined crack with a length of $2l_1$.[22,23] It is assumed here that the path of the two mode I cracks is in the same direction as the applied load. In this case, the following relationship for a stable crack growth can be obtained:

$$\frac{p}{\sqrt{\pi l_2}} = K_{1c} \tag{10.3}$$

where l_2 is the length of the branching crack (Fig. 10-10),

$$p = T_s \sin \theta_k \tag{10.4}$$

and T_s is the resulting force of shear stress σ_s, which causes sliding of the two opposite sides of the inclined crack. By taking the coefficient of friction f into consideration, T_s can be expressed as

$$T_s = 2l_1\sigma_s = -2l_1 q (\sin \theta_k \cos \theta_k - f \sin^2 \theta_k) \tag{10.5}$$

The value of q is negative for compression based on the coordinate system given in Fig. 10-10. Substituting Eqs. (10.4) and (10.5) into (10.3) leads to

$$q = -\frac{\sqrt{\pi l_2}}{2l_1} \frac{K_{1c}}{A(\theta_k, f)} \tag{10.6}$$

where $A(\theta_k, f) = (\sin \theta_k \cos \theta_k - f \sin^2 \theta_k) \sin \theta_k$. It is seen from Eq. (10.6)

that a crack (the value of l_2) will steadily propagate when the applied load increases.

Now consider a homogeneous matrix with one polygonal inclusion, representing an aggregate particle in an infinite matrix, as shown in Fig. 10-11. An initial interfacial crack with length $2l_1$ is assumed to be located along one side AB. This problem can be treated in a similar manner as one with an inclined crack in a homogeneous matrix. But concentrations of shear and normal stresses have to be taken into account. This can be done by introducing coefficients of normal and shear stress concentration, k_n and k_s, respectively. Since the length of the initial inclined crack, $2l_1$, is smaller than the length of the side AB, $2L_1$, the inclined crack initially propagates in mode II (shear mode), as shown in Fig. 10-11*a*. Propagation of the shear crack is governed by

$$q_{\mathrm{II}}^{\mathrm{IF}} = -\frac{K_{\mathrm{IIc}}}{\sqrt{\pi l_1}\, D^{\mathrm{IF}}(\theta_k, f)} \tag{10.7}$$

where

$$D^{\mathrm{IF}} = k_s \sin\theta_k \cos\theta_k - f k_n \sin^2\theta_k \tag{10.8}$$

Superscript IF is used to denote the interface hereafter.

The shear crack reaches the length of $2L_1$ and stops, because further crack

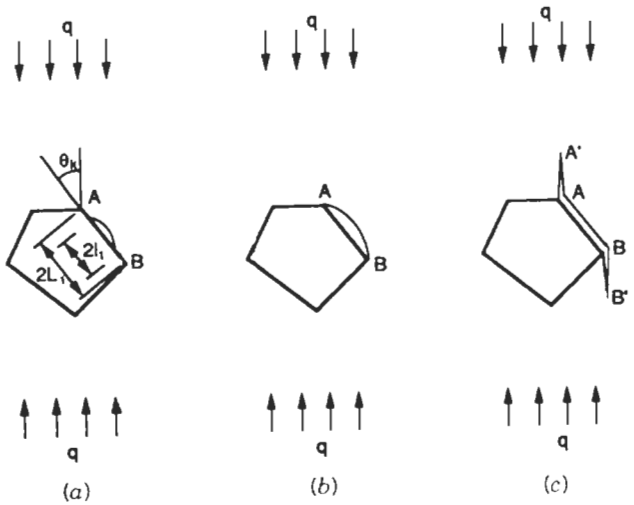

Figure 10-11 Crack propagation in matrix with aggregate: (*a*) an initial crack, (*b*) crack propagation along interface, and (c) crack branching.[20]

propagation in the same inclined direction would take place through the matrix. The mode II critical stress intensity factor of the matrix, K_{IIc}^{M}, is thought to be greater than that of the interface. On the other hand, the value of K_{IIc}^{M} is also thought to be greater than the mode I critical stress intensity factor of the matrix, K_{Ic}^{M}. Therefore, when the inclined crack propagates into the matrix as the load increases, it becomes a mode I crack. The relationship between the compressive load and K_{Ic}^{M} is given by

$$q = -\frac{\sqrt{\pi l_2}}{2L_1}\frac{K_{\mathrm{Ic}}^{M}}{A^{\mathrm{IF}}(\theta_k, f)} \tag{10.9}$$

where $A^{\mathrm{IF}}(\theta_k, f) = D^{\mathrm{IF}}(\theta_k, f)\sin\theta_k$, and l_2 is the distance AA' shown in Fig. 10-11*c*. According to Eq. (10.9), crack length l_2 will steadily increase with increasing load.

For a matrix with two or several aggregates as shown in Fig. 10-12, the same procedure with Fig. 10-11 is repeated. But it is assumed that the branching crack AA' meets a second aggregate as it propagates. Since aggregates usually have higher fracture resistance than the interface in normal concrete, further crack growth will follow the interface MN as a crack of either mode I

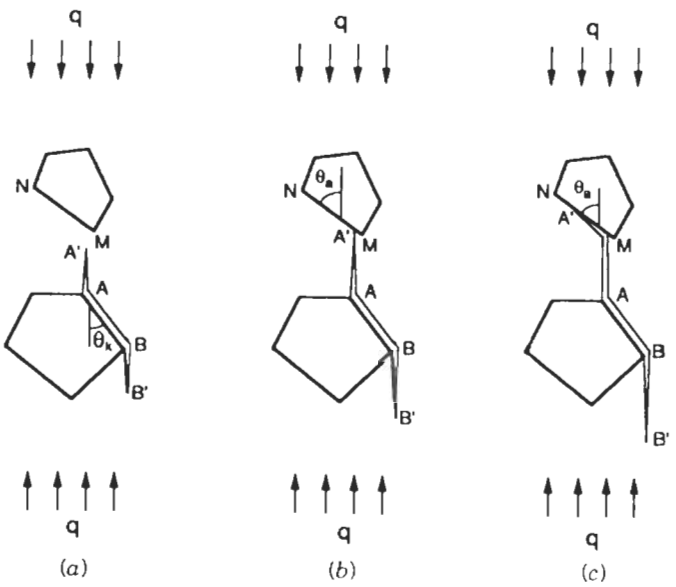

Figure 10-12 Crack propagation in matrix with several aggregates: (*a*) a crack path shown in Fig. 10-11, (*b*) crack meets a second aggregate, and (*c*) crack propagates along interface MN with $\theta_a > 0$.[20]

or mode II. When the crack on the interface MN is mode I, the relationship between the compressive load q_I^{IF} and the mode I interfacial fracture toughness K_{Ic}^{IF} is given by

$$q_I^{IF} = -\frac{2K_{Ic}^{IF}\sqrt{\pi l_2}/L_1}{A^{IF}(\theta_k, f)[3\cos(\theta_a/2) + \cos(3\theta_a/2)] - 3B^{IF}(\theta_k, f)[\sin(\theta_a/2) + \sin(3\theta_a/2)]} \tag{10.10}$$

When the crack on the interface MN is mode II, the relationship between the compressive load q_{II}^{IF} and the mode I interfacial fracture toughness K_{IIc}^{IF} is

$$q_{II}^{IF} = -\frac{2K_{IIc}^{IF}\sqrt{\pi l_2}/L_1}{A^{IF}(\theta_k, f)[\sin(\theta_a/2) + \sin(3\theta_a/2)] - B^{IF}(\theta_k, f)[\cos(\theta_a/2) + 3\cos(3\theta_a/2)]} \tag{10.11}$$

where q_I^{IF} and q_{II}^{IF} are the critical loads to propagate the crack along the path MN as mode I and as mode II, respectively, and $B^{IF}(\theta_k, f) = D^{IF}(\theta_k, f)\cos\theta_k$. Both values of q_I^{IF} and q_{II}^{IF} depend on values of fracture resistances K_{Ic}^{IF} and K_{IIc}^{IF} and are negative for compression.

Zaitsev[21] proposed that whether crack propagation is mode I or mode II depends significantly on the sign of θ_a, as shown in Fig. 10-12. For $\theta_a < 0$ a crack of mode I is to be expected. For $\theta_a > 0$ as given in Fig. 10-12, a crack of mode II is more probable. Zaitsev[21] further indicated that since mode II cracks are facilitated by shear components of applied pressure, the presence of normal confining components of the applied compressive load makes the formation of opening cracks in the interface less likely as compared to the formation of shear cracks. As a consequence, in a material with randomly distributed inclusions (where the probabilities of occurrence of positive and negative values of θ_a are equal), new interfacial cracks will propagate primarily in mode II. This means that a resulting crack running through the whole specimen will contain some interfacial parts. Thus, the resulting crack will be slightly inclined and not exactly parallel to the direction of the applied compressive load, as shown in Fig. 10-13*b*.

More complicated situations including that the crack may propagate into aggregates, which may happen for high-strength concrete and lightweight concrete, have also been discussed by Zaitsev and Wittmann.[20,21]

Zaitsev and Wittmann[20,21] have applied the above procedure to compressive specimens made of hardened cement paste and normal concrete. The obtained cracked patterns for the two types of materials are shown in Fig. 10-13. Zaitsev[21] also applied the proposed method to concrete subjected to a biaxial state of stress and reported that the predicted biaxial failure envelope matches with experimental results quite well.

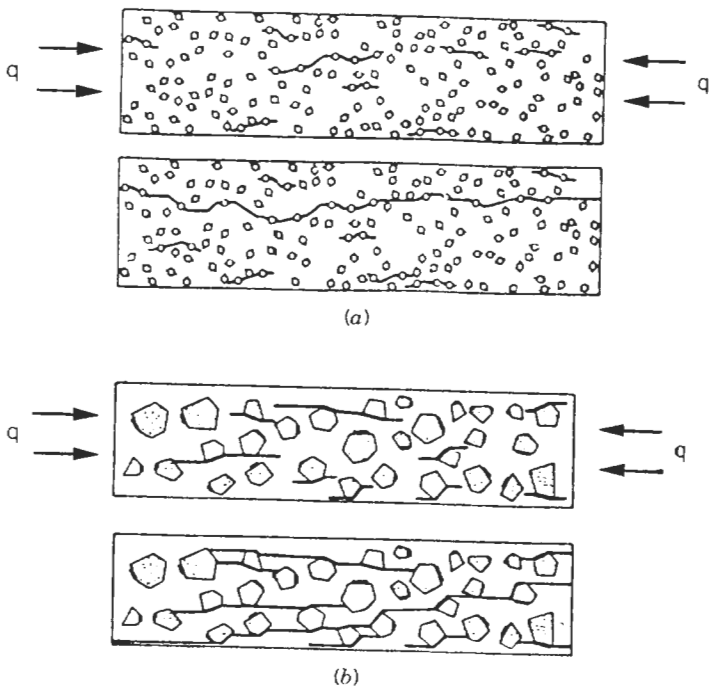

Figure 10-13 Crack patterns for different cementitious materials: (*a*) a hardened cement paste and (*b*) a normal strength concrete.[21]

10.4 MIXED-MODE FRACTURE IN COMPRESSION

The compressive failure of concrete can also be described by using principles of mixed-mode fracture presented in Chapter 8. This has been done by Taşdemir et al.[24,25] for a two-dimensional analysis. Their approach will be presented below.

Consider an infinite-size plate containing an inclined crack, as shown in Fig. 10-14. The length of the inclined crack is $2a$, and the plate is subjected to a uniaxial compressive stress q, where q is defined as negative for compression. The inclined crack may be a bond crack at the interface of an aggregate. After resolution of stresses, the interfacial crack may be considered as subjected to a normal stress σ_β and a shear stress τ_β. Values of σ_β and τ_β are given by

$$\sigma_\beta = -q\sin^2\theta_k \qquad \tau_\beta = -q\sin\theta_k\cos\theta_k \tag{10.12}$$

where θ_k is defined in Fig. 10-14.

Propagation and stability of the interfacial crack could be evaluated using the concept of fracture mechanics. Under compressive loading, the interfacial

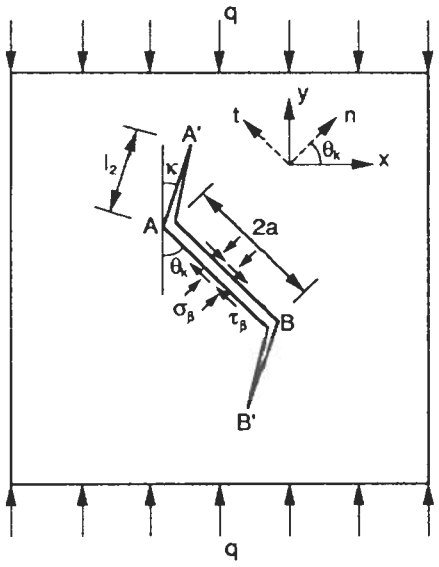

Figure 10-14 Initial crack, stresses at onset of interface debonding and kinks.[24]

crack with the inclination shown in Fig. 10-14 cannot open because the normal stress σ_β is compressive. It cannot close either because the crack surfaces are already in contact. Therefore, the mode I (opening) stress intensity factor at the tip of the interfacial crack, K_I, is zero. This result was verified using a FE analysis. Since the actual crack faces were already in contact, they would only be capable of sliding. The mode II (sliding) stress intensity factor at the tip of the initial interfacial crack is given by[26]

$$K_{II} = -q\sqrt{\pi a}(\sin\theta_k\cos\theta_k - f\sin^2\theta_k) \tag{10.13}$$

where f is the friction coefficient at the interface. It is noted that for sliding to occur, $|\tau_\beta| > f|\sigma_\beta|$. This indicates that there is a critical value of θ_k given by $\theta_{k0} = \operatorname{arccot} f$. Here, K_{II} is zero for $\theta_k > \theta_{k0}$, whereas sliding can occur and the corresponding K_{II} is given by Eq. (10.13) for $\theta_k \le \theta_{k0}$.

The crack will propagate when the applied compressive stress increases. The direction of propagation of the existing crack subjected to a mixed mode is denoted by κ. Generally, κ does not coincide with θ_k. Several criteria have been proposed to determine the value of κ. For example, one may assume that the crack will extend in the direction of the maximum mode I stress intensity factor. The stress intensity factors at the tip of an infinitesimal kink that extends from the initial crack tip at the angle κ can be written as follows[27,28]:

$$K_I^{kink}(\kappa) = -\tfrac{3}{4}K_{II}[\sin(\kappa/2) + \sin(3\kappa/2)] \tag{10.14}$$

and

$$K_{II}^{kink}(\kappa) = \tfrac{1}{4}K_{II}[\cos(\kappa/2) + 3\cos(3\kappa/2)] \tag{10.15}$$

where $K_I^{kink}(\kappa)$ and $K_{II}^{kink}(\kappa)$ are the mode I and mode II stress intensity factors at the tip of the kink, respectively, and K_{II} is given by Eq. (10.13). It is noted that after kinking the value of $K_I^{kink}(\kappa)$ is not zero. Since it is assumed that the crack will extend in the direction of the maximum mode I stress intensity factor, the maximum value of $K_I^{kink}(\kappa)$ occurs at $\kappa = 71°$ for all values of θ_k and can be obtained from $\partial K_I^{kink}(\kappa)/\partial\kappa = 0$. Maji et al.[25] also discussed the use of different fracture criteria for extension of the kink.

An approximate solution has also been proposed by Steiff.[29] His expressions were based on the assumption that crack faces slide parallel to themselves, and the stress intensity factors at the tip of the kink for far-field uniaxial compression are given by

$$K_I^{kink}(\kappa) = -q\sin^2(\theta_k - \kappa)\sqrt{\frac{\pi l_2}{2}} + \frac{3}{4}q\sqrt{\frac{\pi}{2}}\left(\sin\frac{\kappa}{2} + \sin\frac{3\kappa}{2}\right) \cdot (\sin\theta_k\cos\theta_k - f\sin^2\theta_k)(\sqrt{2a + l_2} - \sqrt{l_2}) \tag{10.16}$$

and

$$K_{II}^{kink}(\kappa) = -\frac{q}{2}\sin^2(\theta_k - \kappa)\sqrt{\frac{\pi l_2}{2}} - \frac{q}{4}\sqrt{\frac{\pi}{2}}\left(\cos\frac{\kappa}{2} + 3\cos\frac{3\kappa}{2}\right) \cdot (\sin\theta_k\cos\theta_k - f\sin^2\theta_k)(\sqrt{2a + l_2} - \sqrt{l_2}) \tag{10.17}$$

where l_2 is the length of the kink, as shown in Fig. 10-14. These equations describe the variation of $K_I^{kink}(\kappa)$ and $K_{II}^{kink}(\kappa)$ at the tip of the kink. Equations (10.14) and (10.15) can be obtained by substituting $l_2 = 0$ into Eqs. (10.16) and (10.17). Typical variations of $K_I^{kink}(\kappa)$ and $K_{II}^{kink}(\kappa)$ for $\theta_k = 36°$ and $f = 0.25$ are shown in Fig. 10-15. Note that these equations are based on solutions of an infinite-size plate containing an inclined crack. It is seen that the value of κ for which $K_I^{kink}(\kappa)$ is maximum decreases with increasing value of l_2/a, and this value of κ corresponds to $K_{II}^{kink}(\kappa) = 0$.

Taşdemir et al.[24,25] also used a FE method to analyze finite-size plates sub-

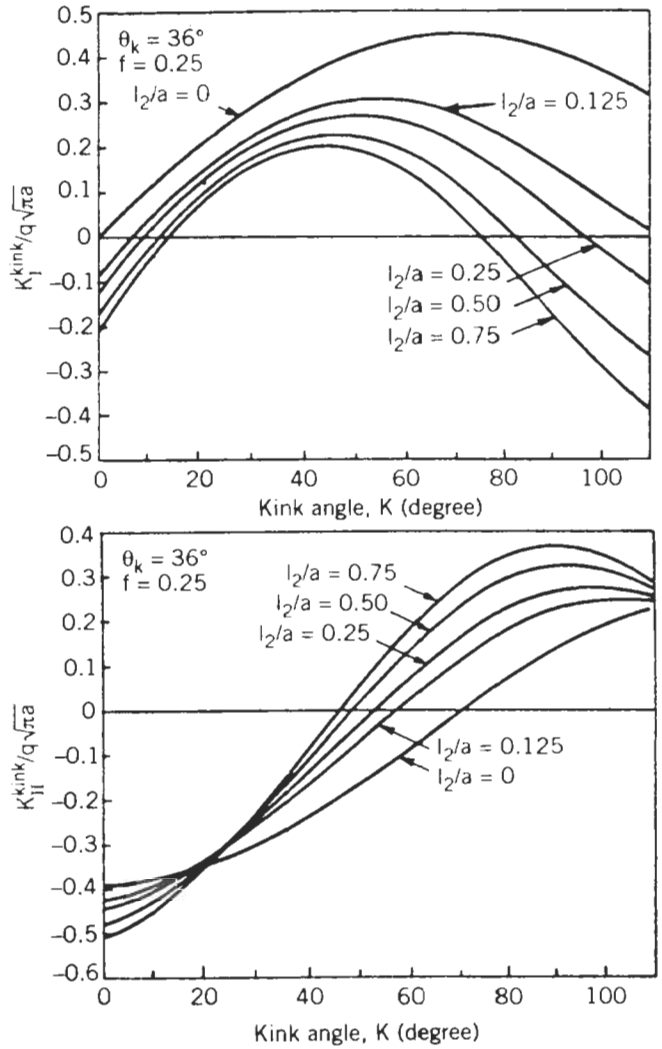

Figure 10-15 Stress intensity factors at tip of kink as function of kink angle.[29]

jected to mixed-mode fracture using the software FRANC, which has been briefly presented in Chapter 5. They also used laser holographic techniques to measure experimentally mixed-mode crack propagation. A two-dimensional elastic analysis was performed using six-noded triangular and eight-noded quadrilateral elements. The dimensions of the specimen and the initial element mesh are shown in Fig. 10-16*a*. The nodes on the top and bottom faces of the crack were fixed in the vertical *Y* direction to simulate absence of closure (Fig.

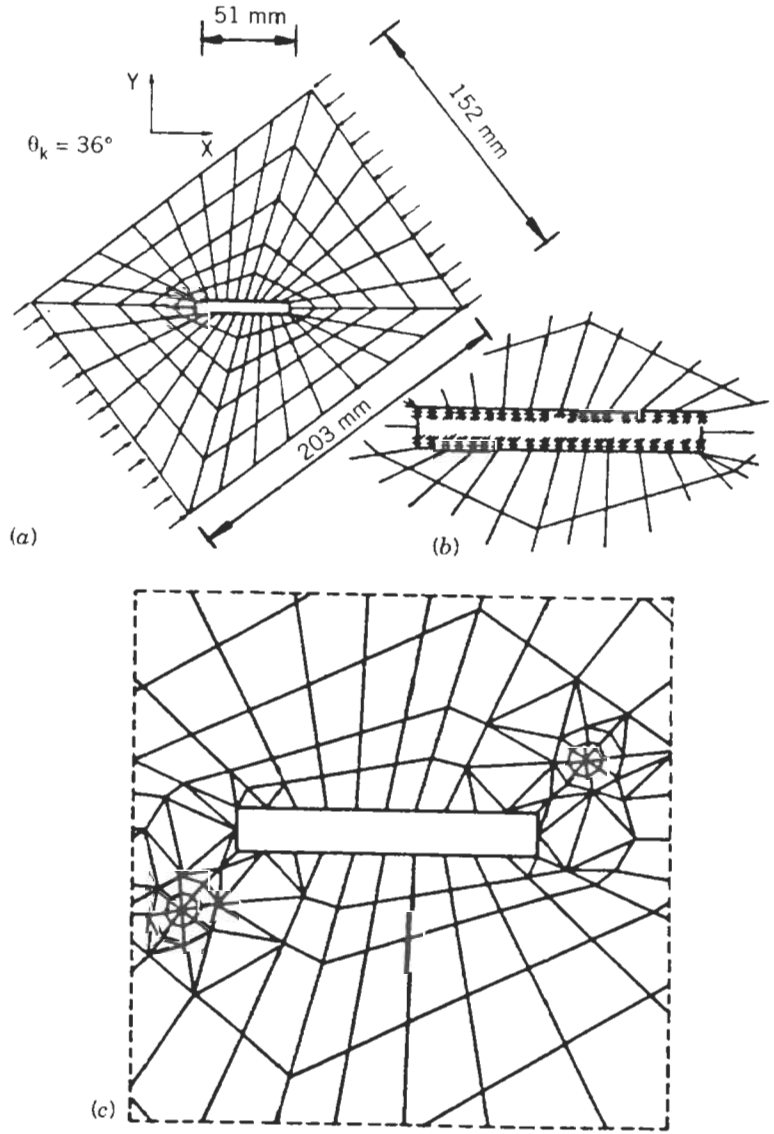

Figure 10-16 Finite element analysis of compressive failure: (*a*) initial mesh, (*b*) boundary condition, and (*c*) mesh showing crack propagation and singular elements.[24]

10-16*b*). One middle node at the upper side of the crack was fixed in the X direction to prevent rigid body translation. Hence, the crack faces were allowed to slide, but not allowed to close and open. The FE analysis was done based on the experimentally observed crack path. The loads were applied at specimen ends to simulate a uniaxial compression. A second set of runs was made where the top and bottom crack faces were loaded with shear tractions to simulate the aggregate matrix friction. The applied shear stress used was of the magnitude of $f\,q\,\sin^2\theta_k$, where $f = 0.25$ was determined experimentally and q was the applied uniaxial compressive stress. These stresses were lumped at the interfacial nodes. Superposition of these two runs resulted in the solutions. A typical mesh with kink extension of about 12.2 mm (0.5 in.) and $\theta_k = 36°$ is shown in Fig. 10-16*c*. Results of the FE analysis were compared with Eq. (10.13) and shown in Fig. 10-17. Note that for this comparison the crack was simulated by a single line representing a sharp crack in the FE mesh. As shown in Fig. 10-17, the results obtained by the FE analysis for the given dimensions are reasonably close to the infinite-size plate solution given by Eq. (10.13). As in previous discussions, it was assumed that the kink will extend

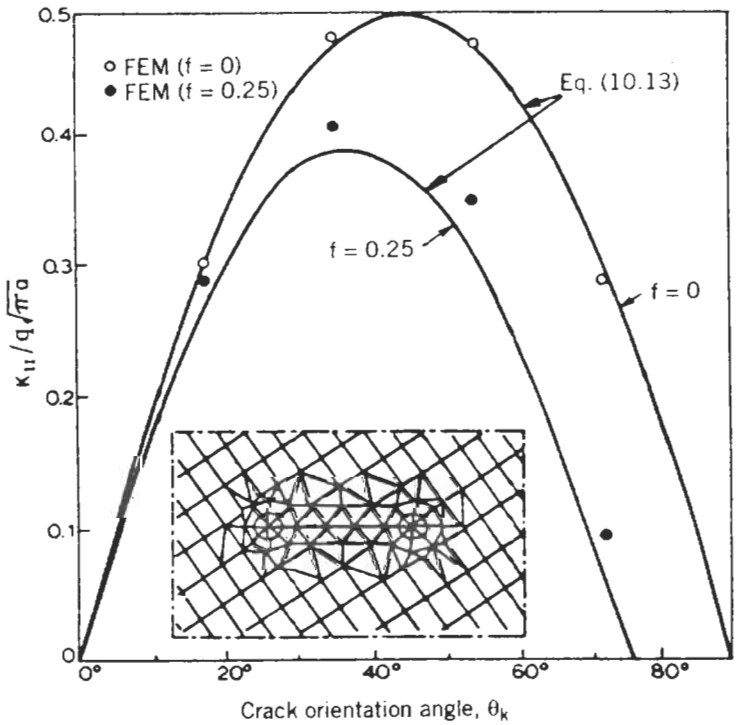

Figure 10-17 Normalized mode II stress intensity factor as function of crack orientation angle.[24]

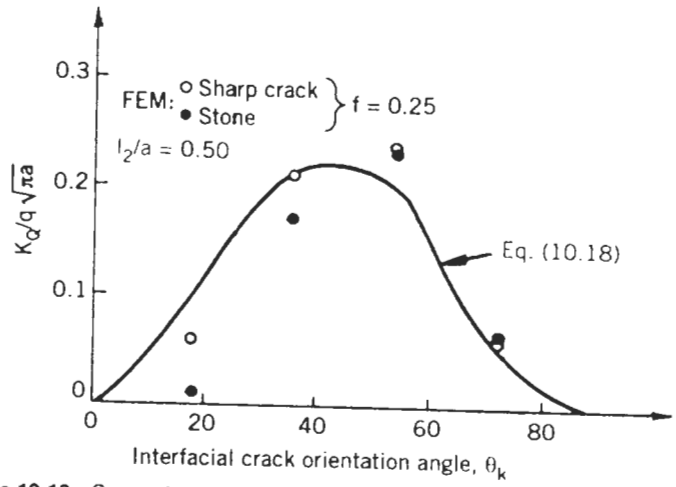

Figure 10-18 Comparison of values of K_Q between Eq. (10.18) and FE analysis.[24]

in the direction of the maximum value of $K_I^{kink}(\kappa)$. This maximum value of $K_I^{kink}(\kappa)$ is denoted by K_Q, which is given by

$$K_Q = \max K_I^{kink}(\kappa) = -1.1547q\sqrt{\pi a}(\sin\theta_k \cos\theta_k - f\sin^2\theta_k) \quad (10.18)$$

based on Eq. (10.16) using the condition $\partial K_I^{kink}(\kappa)/\partial\kappa = 0$. Values of the apparent mode I stress intensity factor, K_Q, obtained by the FE analysis for the plate with given dimension are compared to Eq. (10.18) in Fig. 10-18. For the FE analysis, values of both the sharp crack and the stone–matrix interface are given. The analytical solution correctly predicts the trend for the finite-size plate for the given dimension, but the values of K_Q do not always match. For a given value of the applied stress q, the corresponding value of K_Q can be calculated either by Eq. (10.18) or by a FE method. Based on LEFM, if the value of K_Q is greater than the critical stress intensity factor K_{Ic}, which is a material fracture parameter, the crack will propagate. It is noted that the crack will propagate in the direction of the maximum value of the mode I stress intensity factor, which is determined from the condition $\partial K_I^{kink}(\kappa)/\partial\kappa = 0$. By repeating this procedure for different values of q, a relationship between the applied load and the crack extension can be obtained. Taşdemir et al.[24] also modified an LEFM FE method to take both normal and shear traction forces on cracked faces into account.

10.5 SUMMARY

Mechanisms for compressive failure of concrete specimens have been discussed based on various experimental observations. The compressive failure

is characterized by strain localization. Cracks usually initiate from the interface between the aggregate and cementitious matrix and then coalesce into one or several major cracks that are in the same direction as the applied compressive load. Since the major crack(s) accompanied by the strain localization is in the same direction as the applied compressive load, modeling of the compressive failure using fracture mechanics is more difficult than when compared to the tensile failure of concrete. Several models based on fracture mechanics have been presented to account for this fracture process. It is noted that because of the difficulty in modeling the compressive failure, these models are primarily based on LEFM. Sophisticated models in this area will depend on more understanding of compressive failure mechanisms and on development of new analytical methods.

REFERENCES

1. Hsu, T. T. C., Slate, F. O., Sturman, M., and Winter, G., "Microcracking of Plain Concrete and the Shape of the Stress-Strain Curve," *ACI Journal*, Vol. 60, No. 2, 1963, pp. 209–2224.
2. Shah, S. P., and Chandra, S., "Critical Stress, Volume Change and Microcracking of Concrete," *ACI Journal*, Vol. 65, No. 9, 1968, pp. 770–781.
3. Shah, S. P., and Sankar, R., "Internal Cracking and Strain-Softening Response of Concrete under Uniaxial Compression," *ACI Materials Journal*, Vol. 84, No. 3, 1987, pp. 200–212.
4. Torrenti, J. M., Desrues, J., Benaija, E. H., and Boulay, C., "Stereophotogrammetry and Localization in Concrete under Compression," *Journal of Engineering Mechanics, ASCE*, Vol. 117, No. 7, 1991, pp. 1455–1465.
5. Bascoul, A., Benaija, E. H., Berthaud, Y., Torrenti, J. M., and Zizi, Z., "Analysis of Localization in Concrete through Stereophotogrammetry, Speckle Laser and Replica," *Cement and Concrete Research*, Vol. 23, 1993, pp. 1340–1350.
6. Maji, A. K., and Shah, S. P., "Application of Acoustic Emission and Laser Holography to Study Microfracture in Concrete," in *Nondestructive Testing*, ACI SP-112, edited by Lew, H. S., American Concrete Institute, Detroit, MI, 1988, pp. 83–109.
7. Kupfer, H., Hilsdorf, H. K., and Rusch, H., "Behavior of Concrete under Biaxial Stresses," *ACI Journal*, Vol. 66, No. 8, 1969, pp. 656–666.
8. Kotsovos, M. D., "Effect of Testing Techniques on Post-Ultimate Behavior of Concrete in Compression," *Materials and Structures*, Vol. 16, No. 91, 1983, pp. 3–12.
9. van Mier, J. G. M., "Multiaxial Strain-Softening of Concrete, Part I: Fracture," *Materials and Structures*, Vol. 19, No. 111, 1986, pp. 179–190.
10. Kupfer, H. B., and Gerstle, K. H., "Behavior of Concrete under Biaxial Stresses," *Journal of the Engineering Mechanics Division, ASCE*, Vol. 99, No. EM4, 1973, pp. 853–866.
11. Kotsovos, M. D., "A Mathematical Model of Deformational Behavior of Concrete under Generalized Stress Based on Fundamental Material Properties," *Materials and Structures*, Vol. 13, No. 76, 1980, pp. 289–298.
12. Vonk, R. A., "A Micromechanical Investigation of Softening of Concrete Loaded in Compression," *Heron*, Vol. 38, No. 3, 1993.
13. Mehta, P. K., and Monteiro, P. J. M., *Concrete: Structure, Properties, and Materials*, Prentice-Hall, Englewood Cliffs, NJ, 1993.
14. Nilsen, A. U., and Monteiro, P. J. M., "Concrete: A Three Phase Material," *Cement and Concrete Research*, Vol. 23, 1993, pp. 147–151.
15. Hsu, T. T. C., and Slate, F. O., "Tensile Bond Strength between Aggregate and Cement Paste or Mortar," *ACI Journal*, Vol. 60, No. 4, 1963, pp. 465–486.
16. Shah, S. P., and Winter, G., "Inelastic Behavior and Fracture of Concrete," *ACI Journal*, Vol. 63, No. 9, 1966, pp. 925–930.
17. Hsu, T. C., "Mathematical Analysis of Shrinkage Stresses in a Model of Hardened Concrete," *ACI Journal*, Vol. 60, No. 3, 1963, pp. 371–390.
18. Buyukozturk, O., Nilson, A. H., and Slate, F. O., "Stress-Strain Response and Fracture of a Concrete Model in Biaxial Loading," *ACI Journal*, Vol. 68, No. 8, 1971, pp. 590–599.
19. Palaniswamy, R. G., and Shah, S. P., "A Model for Concrete Subjected to Triaxial Stresses," *Cement and Concrete Research*, Vol. 5, 1975, pp. 273–284.
20. Zaitsev, Y. B., and Wittmann, F. H., "Simulation of Crack Propagation and Failure of Concrete," *Materials and Structures*, Vol. 14, No. 83, 1981, pp. 357–365.
21. Zaitsev, Y. B., "Crack Propagation in a Composite Material," in *Fracture Mechanics of Concrete*, edited by Wittmann, F. H., 1983, Elsevier Science, Amsterdam, 1983, pp. 251–299.
22. Diaz, S. S., and Hilsdorf, H. K., "Fracture Mechanisms of Concrete under Compressive Loads," *Cement and Concrete Research*, Vol. 3, 1973, pp. 363–388.
23. Kotsovos, M. D., and Newman, J. B., "Fracture Mechanics and Concrete Behavior," *Magazine of Concrete Research*, Vol. 33, No. 115, 1981, pp. 103–112.
24. Taşdemir, M. A., Maji, A. K., and Shah, S. P., "Crack Propagation in Concrete under Compression," *Journal of Engineering Mechanics, ASCE*, Vol. 116, No. 5, 1990, pp. 1058–1076.
25. Maji, A. K., Taşdemir, M. A., and Shah, S. P., "Mixed Mode Crack Propagation in Quasi-Brittle Materials," *Engineering Fracture Mechanics*, Vol. 38, No. 2/3, 1991, pp. 129–145.
26. Melville, P. H., "Fracture Mechanics of Brittle Materials in Compression," *International Journal of Fracture*, Vol. 13, 1977, pp. 532–534.
27. Cottrell, B., and Rice, J. R., "Slightly Curved or Kinked Cracks," *International Journal of Fracture*, Vol. 16, No. 2, 1980, pp. 155–169.
28. Horii, H., and Nemat-Nasser, S., "Brittle Failure in Compression: Splitting, Faulting, and Brittle-Ductile Transition," *Philosophical Transactions of the Royal Society of London*, Series A 319, 1986, pp. 337–374.
29. Steiff, P. S., "Crack Extension under Compressive Loading," *Engineering Fracture Mechanics*, Vol. 20, No. 3, 1984, pp. 463–473.

FRACTURE MECHANICS OF CONCRETE: APPLICATIONS OF FRACTURE MECHANICS TO CONCRETE, ROCK, AND OTHER QUASI-BRITTLE MATERIALS

Surendra P. Shah
Walter P. Murphy Professor
Department of Civil Engineering
Northwestern University

Stuart E. Swartz
Professor and Head
Department of Civil Engineering
Kansas State University

Chengsheng Ouyang
Engineer
Office of Materials
Iowa Department of Transportation

A WILEY-INTERSCIENCE PUBLICATION
JOHN WILEY & SONS, INC.
New York / Chichester / Brisbane / Toronto / Singapore